Stick-slip motion and elastic coupling in crawling cells

Alex J. Loosley and Jay X. Tang

Phys. Rev. E **86**, 031908 — Published 10 September 2012

DOI: 10.1103/PhysRevE.86.031908

Stick-Slip Motion and Elastic Coupling in Crawling Cells

Alex J Loosley and Jay X Tang
Department of Physics, Brown University, 182 Hope Street, Providence, RI, USA 02912

Crawling cells exhibit a variety of cell shape dynamics ranging from complex ruffling and bubbling to oscillatory protrusion and retraction. Periodic shape changes during cell migration are recorded in fast moving fish epithelial keratocytes where sticking and slipping at opposite sides of the cell's broad trailing edge generate bipedal locomotion. Barnhart et al. recently proposed a mechanical spring model specifically designed to capture bipedal locomotion in these cells. We extend their model by benchmarking the dynamics of four mechanical configurations against those of crawling keratocytes. Our analysis shows that elastic coupling to the cell nucleus is necessary to generate its lateral motion. We select one configuration to study the effects of cell elasticity, size, and aspect ratio on crawling dynamics. This configuration predicts that shape dynamics are highly dependent on the lamellipodial elasticity, but less sensitive to elasticity at the trailing edge. The model predicts a wide range of dynamics seen in actual crawling keratocytes, including coherent bipedal, coherent non-bipedal, and decoherent motions. This work highlights how the dynamical behaviour of crawling cells can be derived from mechanical properties through which biochemical factors may operate to regulate cellular locomotion.

Further information is available [Barnhart *etal*. Biophys J **98**, 933 (2010)]

Keywords: crawling cells; mechanics; stick-slip; bipedal locomotion; cell motility; cell shape; differential equations

I. INTRODUCTION

Cells are the building blocks of life and their migration is crucial to the biological functions that sustain life. For example, tissue and nervous system formation depends on the coordinated migration of pre-differentiated stem cells [1–3], whereas host immune response depends on leukocyte migration to sites of infection and injury [4, 5]. Thus, understanding the mechanisms of cell migration is important to the field of biology as well as to advancing the frontier of medicine.

Many cells migrate by crawling along a particular substratum. The mechanisms that generate cell crawling dynamics can be generally described in two steps. Step one, actin polymerization occurs at the leading edge of a cell (lamellipodium) causing the cell to protrude forward [6, 7]. New adhesion sites form at the leading edge during this process. Step two, contractile forces generated within the cytoskeleton act to pull the rear of the cell body forward in concert with graded adhesion between the cell and substratum [6]. Cell shape may also play a role in cell crawling. The subject of how cell shape is determined based on intra- and extracellular factors has been studied extensively both experimentally and mathematically [8–13]. There are also studies of the reverse problem in the context of how cell shape affects focal adhesion site formation, traction forces, and cell polarization [14–16], but the specific effects of cell shape on locomotion are as of yet poorly understood.

A variety of cell shape dynamics can occur depending on the type of crawling cells as well as intra- and extracellular factors [9, 17, 18]. For example, leukocytes and fibroblasts exhibit fairly nondeterministic ruffling- and bubbling-like shape dynamics [11, 19, 20]. Other cells, particularly fish epithelial keratocytes, exhibit shape dynamics that appear periodic and coherent [10, 21–23]. Such dynamical periodicity and regularity over many cell lengths of migration make the latter cell type, fish keratocytes, a prototypical system for studying cell shape dynamics and motility [9, 24, 25].

Periodic shape dynamics observed in crawling fish keratocytes are caused by alternating stick-slip motions localized at opposite sides of the cell's broad trailing edge [22, 26]. In fast moving keratocytes, ones that move roughly $0.1\,\mu m/s$ or faster, these sticking and slipping cycles are often observed to be coherent but opposite in phase [24]. Hence, one side of the trailing edge sticks while the other slips in what is known as bipedal locomotion. Barnhart et al. recently introduced a two dimensional mechanical spring model with stick-slip adhesion to capture the dynamics of bipedal locomotion in fish keratocytes. This model consists of four point-like elements located at regions of prevalent shape dynamics of the cell. One element represents the cell leading edge, a region where forces responsible for cell migration are generated by complex cytoskelatal processes such as actin polymerization and retrograde flow [27–30]. Two elements represent opposite sides of the cell trailing edge, regions that exhibit periodic sticking and slipping motions. These three elements are connected by a particular spring configuration that incorporates a fourth element in the central region of the cell. The springs represent either cytoskeletal elasticity or coupling between the cytoskeleton and the nucleus and act to restore overall cell shape in response to mechanical perturbation.

We build on the model by Barnhart et al. by analyzing different possible spring configurations that recapitulate the shape dynamics of crawling fish keratocytes and use the results of this analysis to determine how these dynamics are dependent on cell elasticity, size, and aspect ratio. The central element is now interpreted to be the

cell nucleus and we compare its motion to experimentally observed nucleus lateral displacements. Based on assumptions such as symmetry about the axis of motion and confinement of the nucleus to the central region of the cell, we determine that there are only four viable spring configurations, including the one studied in the previous work. We analyze the dynamics of all four configurations and choose one deemed most mechanically representative of the real cell that also generates realistic dynamics. Using this configuration, we identify three principal parameters representing lamellipodial elasticity, cell length, and cell width that are significant determinants of the amplitude and period of cell shape oscillations. Varying these principal parameters over a realistic range, we show that this simple spring model generates shape dynamics corresponding to coherent bipedal, coherent non-bipedal, and decoherent crawling cells.

II. METHODS

A. Model overview

Similar to the previous work by Barnhart *et al.* [24], we model the fish keratocyte in 2-D using four elastically coupled point-like elements representing different dynamic regions of the cell. To introduce the assumptions and physics underlying this elastic coupling model, we begin with a demonstrative 1-D version illustrated in Fig. 1 *A*. In this version, the front end, represented by x_1, extends forward with velocity v_f (dashed line indicates cell protrusion). It is assumed that this forward propulsion is maintained by the formation of new adhesions to the substrate. The trailing edge of the cell, at position x_2, is coupled to the front by a spring of equilibrium length L_0 and stiffness K that is representative of the cell length and elasticity of the actin cytoskeleton, respectively. The assumption of a linearly elastic cytoskeleton is justified under physiologically normal strains [31, 32].

The trailing edge element experiences two types of drag forces, adhesion (sticking) and viscous shear (slipping). Adhesion occurs due to stochastic binding and unbinding of adhesion proteins between the cell and its substrate [23, 33, 34]. The associated free energy landscape that influences the adhesion proteins is modelled by quadratic potential wells with minima corresponding to binding sites on the substrate [33, 34]. Equivalently, transient attachments of adhesion proteins between the cell and its substrate can be thought of as springs (see Fig. 1 *A* overlay). If the average spring constant for each adhesive bond is κ, then the force against the direction of motion due to a particular adhesion bond that forms at time t_i^{bind} is approximately

$$F_i \approx \kappa \dot{x}_2 (t - t_i^{bind}), \tag{1}$$

where $\dot{x}_2$ is the trailing edge speed, t is time, and index i refers to the i^{th} adhesion bond. Equation 1 is valid only between the binding time, t_i^{bind}, and some particular unbinding time, t_i^{unbind}, when the spring detaches. Times t_i^{bind} and t_i^{unbind} are stochastic variables with distributions that depend on the trailing edge velocity [33]. Upon summation over all binding events, the time averaged adhesive drag force is found to scale linearly with $\dot{x}_2$ and κ at low trailing edge speed. At sufficiently high trailing edge speed, the adhesive force vanishes because adhesion proteins do not spend enough time within the capture region of conjugate binding sites to form bonds. At high trailing edge speed, the drag force is also thought to scale linearly with $\dot{x}_2$ due to the hydrodynamics of low Reynolds number viscous shear. However, the constant of proportionality is much smaller than that associated with adhesion.

One can define two drag coefficients: α for slipping, and β for sticking, which incorporates κ. The overall stick-slip drag force as a function of trailing edge velocity is modelled by

$$F_d[\dot{x}_2] = \begin{cases} -\beta \dot{x}_2 \,, & \dot{x}_2 < v_1 \\ \frac{v_1 - \dot{x}_2}{v_1 - v_2}(\beta v_1 - \alpha v_2) - \beta v_1 \,, & v_1 < \dot{x}_2 < v_2 \\ -\alpha \dot{x}_2 \,, & v_2 < \dot{x}_2 \end{cases} \tag{2}$$

Here, sticking occurs when $\dot{x}_2 < v_1$ (stick domain) due to adhesion bonds, slipping occurs when $\dot{x}_2 > v_2$ (slip domain), and some combination of sticking and slipping occurs when $v_1 < \dot{x}_2 < v_2$ (transition domain). In the transition domain, the drag force is modelled by linear interpolation [Fig. 1(*b*)] though the shape of the curve in this transition region has little effect on the resulting dynamics.

An additional consideration taking into account the time it takes the cell to switch from sticking to slipping, and vice versa, is captured by a small inertia-like parameter, g, the physical meaning of which is fully discussed in Ref. [24]. Including this g-factor, the equations of motion for the one dimensional model are

$$\dot{x}_1 = v_f \tag{3}$$

$$g\ddot{x}_2 - F_d\left[\dot{x}_2\right] - K(L - L_0) = 0 \tag{4}$$

where $L = x_1 - x_2$, and $F_d[\dot{x}_2]$ is the stick-slip drag force given in Eq. 2.

Solutions to Eqs. 3 and 4 are limit cycles in the phase space of scaled cell-length, $\frac{L-L_0}{K}$, and trailing edge velocity, $\dot{x}_2$. Fig. 1(*c*) shows two such shape-cycle trajectories plotted in this phase space. When the inertia-like term is removed ($g = 0$), spring force must be balanced by drag force. In the stick domain ($\dot{x}_2 < v_1 < v_f$), the trailing edge velocity is less than the velocity of the extending leading edge. Consequently, the spring representing cell length extends, increasing the forward force applied to the trailing edge element. As this force increases, so too does the trailing edge velocity. When $\dot{x}_2$ increases to be infinitesimally greater than v_1, the sticking drag force is insufficient to balance against the forward force of the

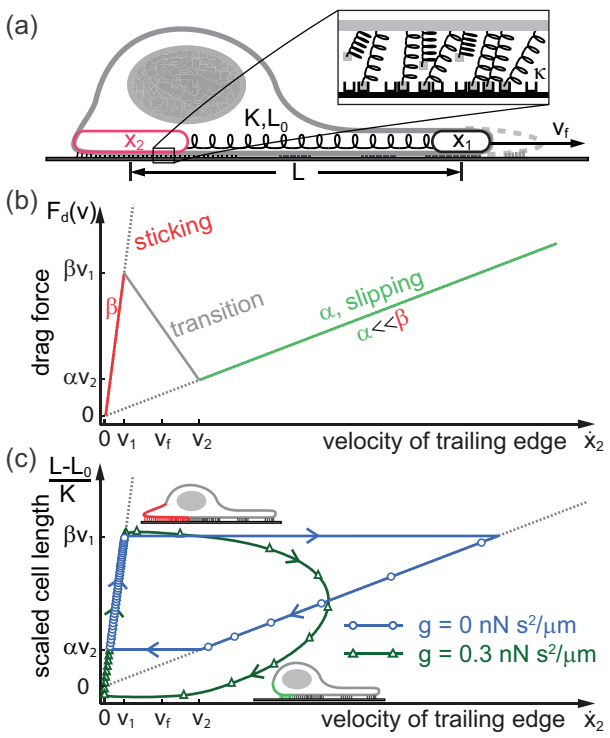

FIG. 1. (Color online) 1-D crawling cell model. (a) The leading edge, x_1, moves forward with constant velocity, v_f, representing a region where the lamellipodium extends forward. The trailing edge, x_2, is elastically coupled to the leading edge by a spring of elasticity K and rest-length L_0 representing cytoskeletal elasticity and extension, respectively. A stick-slip drag force underneath the trailing edge is modelled by many small springs with average spring constant κ. (b) Drag force-velocity curve. At low trailing edge velocity, $\dot{x}_2 < v_1$ (stick domain), drag force is generated by adhesion complexes forming between the cell membrane and substrate. To good approximation, such adhesion generated drag force scales linearly with velocity characterized by drag coefficient, β. At high trailing edge velocity, $\dot{x}_2 > v_2$ (slip domain), adhesion complexes no longer form. The drag force in this domain is purely viscous in nature and characterized by the relatively small linear drag coefficient, α ($\alpha \ll \beta$). At intermediate velocities, $v_1 < \dot{x}_2 < v_2$ (transition domain), drag force is generated by a mixture of the sticking and slipping mechanisms. The overall drag-velocity curve is continuous in all domains. (c) Cell length-velocity phase space trajectories with and without the inertia term, g. Data points are separated by a constant time step equal to one fiftieth of the limit cycle period ($T/50$). Therefore, rapid changes in velocity and cell length are noted by relatively large distances between consecutive data points.

spring. The trailing edge therefore accelerates instantaneously until force balance is re-established by the slipping drag force (cyan trajectory). When the inertia-like term is applied, e.g. $g = 0.3\, s^2\, nN/\mu m$, force balance is not instantaneously required and abrupt acceleration does not occur. Hence, the limit cycle trajectory in phase space appears rounded (green trajectory). In both cases, the shape of the drag force-velocity curve in the transition domain (Eq. 2, $v_1 < \dot{x}_2 < v_2$) has negligible effect on the resulting dynamics because the dynamical variable $\dot{x}_2(t)$ remains within this domain over a duration that is negligible compared to the limit cycle period.

This model is extended into 2-D as shown in Fig. 2. The trailing edge, where bipedal locomotion occurs, is represented by two elements located at $\vec{x}_l$ and $\vec{x}_r$. The drag force in Eq. 2 is vectorially applied to both elements in the opposite direction of motion. The nucleus is represented by an element located at $\vec{x}_n$. Drag on this element is intermediate between sticking and slipping drags associated with the trailing edge. The front element that drives the system forward is now represented by location vector $\vec{x}_f$, instead of $\vec{x}_1$ as in the 1-D model. Later in this work, we replace the front element with a rod-like element that better represents the wide extent of the protruding edge of the lamellipodium. Spring and drag forces are combined into a set of 2-D equations of motion. The 2-D equations of motion and a discussion about initial conditions is provided in the supplemental material. A reference diagram for this model is shown in Fig. 2(b) listing the spring constants, spring lengths, and drag coefficients. Cell lengths Δy_l and Δy_r are two of the dynamical variables used to characterize bipedal locomotion. They are defined as the distance from the front element to the left and right trailing elements, respectively, projected onto the axis of forward motion (y-axis). Fig 2(b) also defines a cell width, Δx, as the distance between the trailing edge elements projected on the axis perpendicular to forward motion (x-axis).

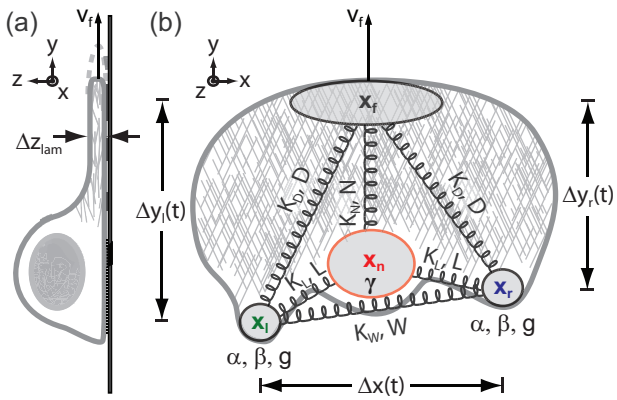

FIG. 2. (Color online) Schematic of four element elastic coupling model in 2-D. (a) Side profile of the cell, Δz_{lam} is the lamellipodium thickness. (b) Top down reference diagram of the 2-D elastic coupling model. Elements, depicted by ovals, are located at $\vec{x}_f$, $\vec{x}_l$, $\vec{x}_r$, and $\vec{x}_n$. The front element moves with constant velocity $\vec{v}_f$. Spring lengths and elasticity are indicated next to each spring. Element specific drag coefficients are shown in rectangular boxes. The cell is modelled symmetrically about the axis of forward motion, $\vec{v}_f$. Cell lengths Δy_l and Δy_r are defined as the distance between $\vec{x}_f$ and either $\vec{x}_l$ or $\vec{x}_r$ respectively, projected onto the axis of forward motion.

B. Simulation methods and criteria for characterizing dynamics

Solutions to the 2-D equations of motion (Eqs. 1-4, 7, 8 in the supplemental material) were found by numerical integration using the Runge-Kutta algorithm built into MATLAB R2010b (The Mathworks, Natick, MA). A dynamical solution was considered periodic if the left and right side cell length dynamics stabilized into periodic motion within 800 s. For a typical limit cycle period of 40 s, this equates to 20 periods. Fourier transformation was used to measure frequency. For solutions deemed periodic, phase differences between Δy_l and Δy_r were calculated. Frequency was determined by locating the first harmonic of the Fourier transform while phase was determined by the complex argument of the Fourier transform at this harmonic. Fourier transforms were calculated using the MATLAB fast Fourier transform algorithm. We also measured amplitudes of cell length modulation and nucleus lateral displacement, which is defined as the distance of the central element, $\vec{x}_n$, from the axis of forward motion. Simulation dynamics were considered bipedal if cell length oscillations were periodic and the phase difference between Δy_l and Δy_r was between 0.45 and 0.55 periods. Dynamics were otherwise labelled as either periodic or irregular. Bipedal dynamics are said to be realistic if the following three conditions are satisfied, which are based on experimental observations of fish keratocyte dynamics discussed in the supplemental material (Figs. S1 and S2):

1. amplitude of cell length modulation from 1 to 3 μm;
2. amplitude of nucleus lateral displacement from 0.3 to 1.2 μm;
3. period of limit cycle from 30 to 70 s.

Throughout this paper, simulation results are benchmarked against experimental analysis of keratocytes discussed in the supplemental material.

C. Choice of model parameters

Parameter values for α, β, v_1, and v_2 were chosen based on estimates made from the previous work [24]. A summary of the parameters used in this model, including numerical ranges based on measurements of cell size, aspect ratio, and other dynamical quantities, is shown in Table I. The elastic modulus of a keratocyte, E, has been measured to be between 10 and 150 $nN/\mu m^2$ [31, 35, 36], and is thought to increase from anterior to posterior. The model was analyzed over this range of E by varying the stiffness of springs that correspond to different regions of the cell. These spring stiffnesses were calculated using the relation,

$$k = \frac{ES}{d}, \tag{5}$$

where S is the cross section area and d is the spring length. For example, to calculate K_D, we set $S \approx L\Delta z_{lam}$ and $d = D$ (see Fig. 2). Using $\Delta z_{lam} \sim 0.1\mu m$ [36, 37] and $L/D \sim 0.5-1$ based on keratocyte cell shapes measurements (see supplemental material) [9, 10, 24] yields a spring constant range $K_D \sim 0.5 - 15nN/\mu m$. The viability of this model was tested using spring constants varied from 0 to $10\,nN/\mu m$. Spring lengths were chosen in conjunction with spring constants so that simulated cell width and length corresponded to the shapes of fish keratocyte cells observed in previous publications (see supplemental material), though cell shape range need not have been restricted in this manner.

D. Simulation benchmarking

Phase contrast movies of eleven motile fish keratocytes, five undergoing bipedal locomotion, were analyzed to measure cell sizes, aspect ratios, and other dynamical quantities used to benchmark simulation dynamics (see Fig. S1). These movies were obtained from the supplemental materials of Refs. [9, 10, 24, 38]. Movies were converted to image sequences using Virtual Dub (Avery Lee) or MPEG Streamclip (Squared 5) depending on file format. Custom MATLAB software was used to determine image by image cell symmetry axes and trajectories of the leading edge, trailing edge, and nucleus centroid. We measured nucleus lateral displacement to be the distance from the nucleus centroid to a line of best fit (see Fig. S2). Experimental cell length oscillations were measured as the distance between the center of the leading edge and either of the trailing edge elements, projected onto the cell symmetry axis. There are minor discrepancies between these measurements and simulated cell length oscillations because the experimental symmetry axis does not always correspond to the axis of forward motion. An example of cell length oscillation measurements is shown in Movie S1.

III. RESULTS

A. Viable spring configurations

There are several ways to elastically couple the elements that make up the two dimensional model [Fig. 2(b)], in particular by adding or removing springs to form different spring configurations. By assuming symmetry about the axis of forward motion and by requiring the cell to maintain a reasonable shape with width and length comparable to observations, the number of possible configurations is constrained to the four illustrated in Fig. 3(a). Config. 1 is the simplest possible configuration that can generate bipedal locomotion whereas Configs. 2 through 4 generate bipedal locomotion with one added element that represents the cell nucleus. The dynamics

of all four configurations are discussed at length in the supplemental material (see Fig. S3).

Briefly, Config. 1 can generate dynamics that are similar to bipedal locomotion, though the single direct coupling between trailing edge elements through the K_W spring leads to aberrant motions at the trailing edge. Specifically, slipping of one trailing edge element extends the K_W spring causing momentary aberrant slipping of the opposite trailing edge element. There is also no possibility for Config. 1 to describe the observed lateral displacement of a keratocyte nucleus. Adding a central element allows for indirect elastic coupling between the trailing edge elements that supplements the direct K_W connection. Config. 2 is like Config. 1 except a central element is added and all four elements are directly coupled to each other. This configuration can generate bipedal locomotion and realistic nucleus lateral displacement if one interprets the central element to be the nucleus. However, such dynamics are not robust under parameter variation compared to configurations with fewer springs. Config. 2 works best near the $K_D \to 0$ or $K_W \to 0$ limits, i.e. Config. 3 or Config. 4, respectively.

Config. 3 is the spring arrangement considered by Barnhart et al. They found that stable bipedal locomotion occurs over a range of K_W and g-values. During bipedal locomotion, the central element, $\vec{x}_n$, oscillates in the lateral direction entrained to the bipedal limit cycle. Although Config. 3 produces realistic bipedal dynamics, we have no physical interpretation of a spring directly coupling the trailing edge elements. In contrast, we introduce an alternative configuration, Config. 4, and use a spring orientation argument to suggest that it better captures the mechanical properties of the actin cytoskeleton. Config. 4 is different from Config. 3 by the removal of the K_W spring ($K_W = 0$), and the addition of two springs that couple each trailing edge element to the leading edge element ($K_D > 0$). In this model, the K_D springs tend to orient with angles similar to the known orientation angles of actin filaments that make up the lamellipodial actin network in keratocytes [39, 40]. Specifically, actin filaments in keratocytes under physiological conditions show long range orientation order with angles between $\pm 25^o$ and $\pm 45^o$ with respect to the direction of leading edge protrusion. The K_D springs capture the anisotropy of network elasticity [41] in the direction parallel to filament orientation. Cell width is now maintained by both the K_D and K_L springs, instead of spring K_W as in Config. 3. Springs, K_L, coupling the trailing edge to the nucleus can be interpreted in the context of the contractile actin-myosin bundle at the rear of the cell [42], though a K_W spring can also be interpreted in the same way.

Configuration 4 generates dynamics similar to those of Config. 3, in some cases with a slightly larger nucleus lateral displacement closer to experimentally observed values. An example time lapse showing the dynamics of Config. 4 is shown in Fig. 3(b). Cell length and nucleus lateral displacement time plots corresponding to the time lapse are shown in Fig. 3(c) and (d), respectively. In this example, the nucleus undulates laterally in a series of exponential decays that have a period of 40.5 s, and an amplitude of 0.6 μm, consistent with observations. Nucleus lateral displacement can be made more sinusoidal if

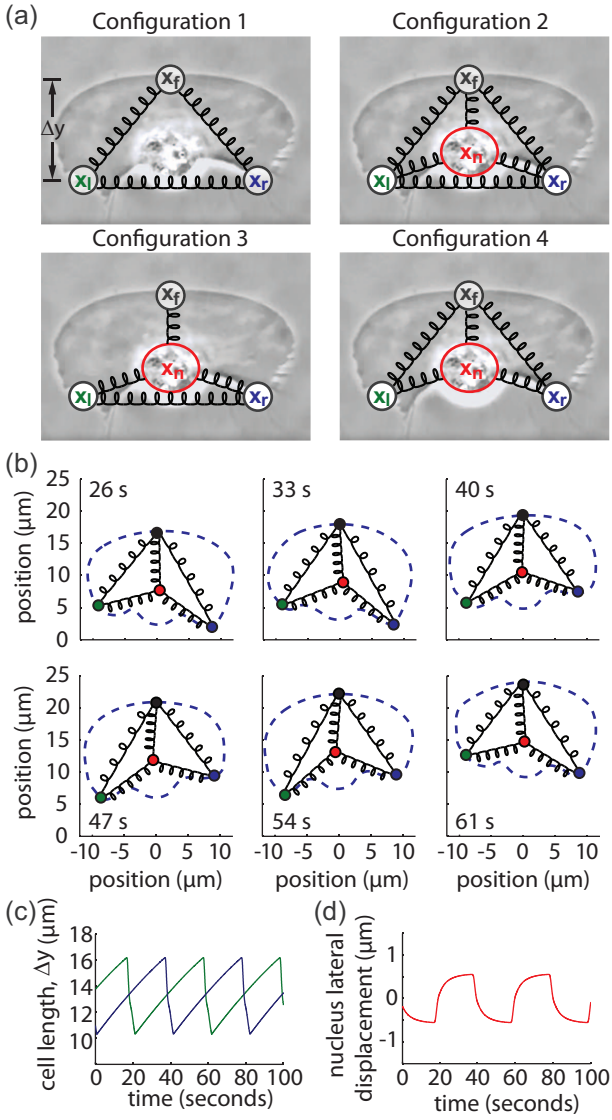

FIG. 3. (Color online) Viable 2-D spring configurations and the dynamics of Config. 4. (a) Diagrams of the four viable 2-D spring configurations. Each viable configuration maintains reasonable cell shape and is symmetric about the axis of forward motion. Config. 4 is the preferred configuration proposed in this work. (b) Time lapse of the simulated dynamics of Config. 4. showing bipedal locomotion. The time lapse is shown in 7 s increments and corresponds to time plots of cell length and nucleus lateral displacement shown in (c) and (d). This simulation corresponds to a cell with a time averaged length and width of 13 and 19 μm, respectively. The amplitude of length oscillations is 3.0 μm with a period of 40.5 s. The amplitude of nucleus lateral displacement is 0.6 μm. A continuous motion time lapse of this simulation is found in Movie S2. Parameters corresponding to this simulation are listed in Fig. S3.

the drag force (parameter γ) is reduced compared to the spring forces acting on the nucleus, though it is unclear if this would be more realistic.

To assess the viability of Config. 4, we investigated how its bipedal dynamics changed in response to varying mechanical parameters, K_D, K_L, and K_N, drag parameters, α, β, γ, and g, and cell shape parameters, D, L, and N. Fig. 4, (a) and (b) are phase diagrams of the dynamical responses plotted in the g-K_D and g-K_L spaces, respectively. Hatched areas indicate regions of realistic bipedal dynamics for two choices of drag coefficient γ. The dynamical response is characterized by amplitudes of cell length and nucleus lateral displacement oscillations (blue curves), and the overall limit cycle period (green curve) shown in Fig. 4, (c) and (d). Bipedal locomotion occurred for spring stiffnesses, $K_D \gtrsim 0.4\ nN/\mu m$ and $K_L \gtrsim 0.5\ nN/\mu m$. The model fails at lower spring stiffnesses because there is not enough rigidity between elements to maintain normal cell shape. In the case of lower elasticity, $K_L < 0.5\ nN/\mu m$, element $\vec{x}_l$ can unrealistically swing over from the left side to the right side of the cell (and vice versa for element $\vec{x}_r$). In the normal cell shape regime, response characteristics changed very little under variation of K_L, in contrast to variation of K_D. Therefore, we identify lamellipodial spring stiffness, K_D, as a principal parameter that tunes the length- and time-scales of limit cycle behaviour, more so than other mechanical parameters in this model. Fig. S4 in the supplemental material shows that response characteristics are also sensitive to variation of sticking coefficient, β, though less sensitive to variation of drag coefficient, γ, and inertia-like parameter, g.

Not shown in Fig. 4 or in the supplemental material is the effect of spring elasticity K_N on the dynamics of Config. 4. Spring K_N in conjunction with drag on the nucleus can be used to fix the average displacement between the front element and the nucleus element. Spring elasticity K_N is required to be greater than 1 $nN/\mu m$ in order to maintain cell shape. As K_N increases, the nucleus element is drawn toward the front of the cell, thus also drawing the trailing edge elements inwards. Bipedal locomotion still occurs with slightly altered period and amplitudes.

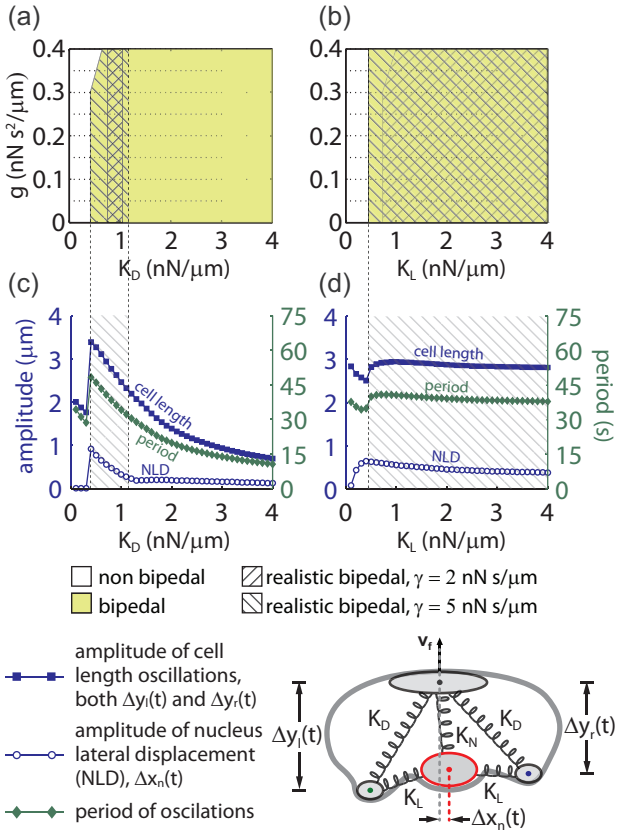

FIG. 4. (Color online) Dynamical responses of Config. 4 with respect to parameters K_D, K_L and g. The green shaded regions of the $g - K_D$ (a) and $g - K_L$ (b) parameter spaces indicate bipedal dynamics and hatch patterns indicate realistic bipedal dynamics for two choices of γ. (c, d) Amplitudes of cell length and nucleus lateral displacement (NLD) oscillations (blue curves), as well as the limit cycle period (green curve), plotted against mechanical parameters K_D and K_L. Lamellipodium spring elasticity, K_D, significantly alters limit cycle amplitudes and periods, whereas trailing edge spring elasticity, K_L, does not. The model fails when either spring constant is too low ($\lesssim 0.5\ nN/\mu m$) where then point-like elements delocalize leading to a loss of normal shape. In each chart, parameters that are not varied are listed in Fig. S3 under Config. 4.

B. Crawling dynamics depend on cell aspect ratio

Using Config. 4, we systematically varied lamellipodial elasticity, cell size, and cell aspect ratio to analyze their effects on crawling dynamics. Cell width was varied by changing spring length L (width $\approx 2L$), and lamellipodial elasticity was varied via the K_D parameter, which is the principle mechanical parameter that tunes the dynamics of this model. Two different cell lengths were studied based on the experimental cell length distribution in Fig. S1 (a): short, $\langle \Delta y(t) \rangle = 11\ \mu m$ ($N = 8\ \mu m$), and long, $\langle \Delta y(t) \rangle = 16\ \mu m$ ($N = 12\ \mu m$). Mathematically, diagonal spring length D was made functionally dependent on L, N, and K_D in order to hold the cell length constant under variation of the dependent parameters (see Fig. 2).

The results of this analysis are shown as cases 1 and 2 in Fig. 5. Case 3 is a modification of Config. 4 where a rod-like element is used at the leading edge instead of point-like element, $\vec{x}_f$. In the sense that the K_D springs represent a center of mean elasticity on the two sides of the lamellipodial actin network, it is likely more realistic that these springs should couple to two points at the leading edge that are symmetrically displaced from the axis of symmetry, instead of to a point at $\vec{x}_f$. A rod-like element allows us to modify the endpoints of springs K_D in just this way. The rod also better aligns the K_D

springs with the known long range angular orientation of the cytoskeleton discussed above. The modified equations of motion for this configuration, which we call the handlebar model, are found in the supplemental material.

Diagrams of the three cases discussed above are shown in Fig. 5(a). For each case, we investigated the effects of varying cell width and lamellipodium elasticity. Dynamical output is characterized by amplitude of cell length oscillations and dynamical behaviour as shown in Fig. 5(b) and (c) respectively. The amplitude maps can be broken down into three key regions. Regions of red indicate relatively large amplitudes (3-10 μm). These amplitudes are greater than those of most coherent keratocytes and occur when lamellipodium elasticity is low, causing the trailing edge to stick longer. Regions of dark blue indicate relatively small amplitudes (0-1 μm). These amplitude describe most smooth gliding keratocytes that have small stick-slip events observed at the trailing edge (for example, in Movie S1). Regions of both light blue and yellow indicate amplitudes of realistic bipedal locomotion (1-3 μm). In cases 1 and 2, there appear to be "anomalous" amplitude variations for wide cells when $K_D \gtrsim 6\ nN/\mu m$. The phase diagrams indicate that these anomalous regions of the amplitude maps correspond to irregular behaviour [Fig. 5(c)]. Such regions could represent the phase space for fast moving decoherent cells. Smooth gliding cells are described by all dynamical behaviours with small amplitudes. Exceptions shown here are cells that fail to maintain proper cell shape, which are indicated in white at the top-right corner of the phase diagram for case 1, although there are other examples beyond these parameter ranges. Realistic bipedal locomotion occurs in regions of overlap between those labelled bipedal on the phase diagrams and those where amplitudes of cell length oscillations fall between 1 and 3 μm. Overall, one can use the phase diagrams in conjunction with the amplitude maps to characterize the dynamical responses of the model. These diagrams describe how cell crawling dynamics are dependent on cytoskeletal elasticity, extension, and cell aspect ratio.

IV. DISCUSSION

Cell motility models typically consist of a set of dynamical equations that describe the biochemistry (i.e., diffusion and flow of biomolecules that regulate myosin motors, actin polymerization, etc.) and/or the biomechanics (i.e., adhesion between cell and substrate, cortical tension, etc.) of a system to varying degrees of complexity [12, 13, 24, 29, 43–46]. That a simple mechanical model involving only four elements coupled by passive springs is able to significantly recapitulate the motion of these highly complicated systems is surprising. There are alternative models describing the shape dynamics of keratocytes, such as one proposed by Ziebert *et al.* [46], in which cell length oscillations result from filament orientation and overall cell shape. In another model proposed by Barnhart *et al.* [13], the implications of substrate adhesion strength on keratocyte motility were studied by considering the interplay between actin polymerization, myosin II transport, myosin II generated actin retrograde flow, and linear adhesion forces between the cell and its substrate. Their model generates the characteristic cell shapes and migration speeds recorded in fish keratocytes, but it does not account for bipedal locomotion. Our model describes general cell crawling dynamics and its dependency on mechanical properties but does not account for the specific effects of adhesion strength because the physics of adhesion at the leading edge and other more complicated factors such as actin polymerization and actin retrograde motion are all contained in the self-propulsion parameter, $\vec{v}_f$, which prescribes the cell's locomotion speed. We ignore the finer details of these factors in exchange for a simple model to study cell crawling dynamics with a focus distinct from that of Ref. [13].

In our analysis of cell crawling movies from previous publications, it is apparent that the leading edge velocity of bipedally crawling cells fluctuates, although these fluctuations are not as large as stick-slip induced velocity fluctuations at the trailing edge. As such, assuming a constant velocity, $\vec{v}_f$, at the leading edge is an oversimplification. Instead, one could model the forward propulsion by introducing a propulsion force in place of velocity $\vec{v}_f$. Such a force would have to be anchored by adhesion formation under the ventral surface of the cell that would lead to a net forward spring force large enough to propel the trailing edge elements into the slipping domain without allowing the cell to stall. The force at the leading edge could be calculated from empirical force-velocity relations such as the one recently measured by Heinemann *et al.* [37] using slow crawling keratocytes. In this case, the load force would be assumed to scale with the total spring force acting against leading edge and the force-velocity relation would then be used to calculate the leading edge velocity. At this time, however, it is unknown how the force-velocity curves measured by Heinemann et al. are different from those of fast crawling keratocytes, which have distinctly different leading edge characteristics. Measurements and models of force-velocity curves for other systems such as listeria [29, 47] are strikingly different from those in Ref. [37]. In listeria, the protrusion velocity is nearly independent of load under high loading conditions, whereas the opposite is true for slow crawling keratocytes. Given the variability of force-velocity relationships in the literature, we stay with the constant velocity approximation as a first step to mechanically modelling cell dynamics, instead of invoking a protrusion velocity that requires knowledge of a force velocity curve.

Beyond investigating the stick-slip dynamics of the keratocyte trailing edge, our analysis also probes the role of the cell nucleus. It is well known that epithelial keratocytes are complex systems with mechanical properties that depend on the actin cytoskeleton [48–50], but here

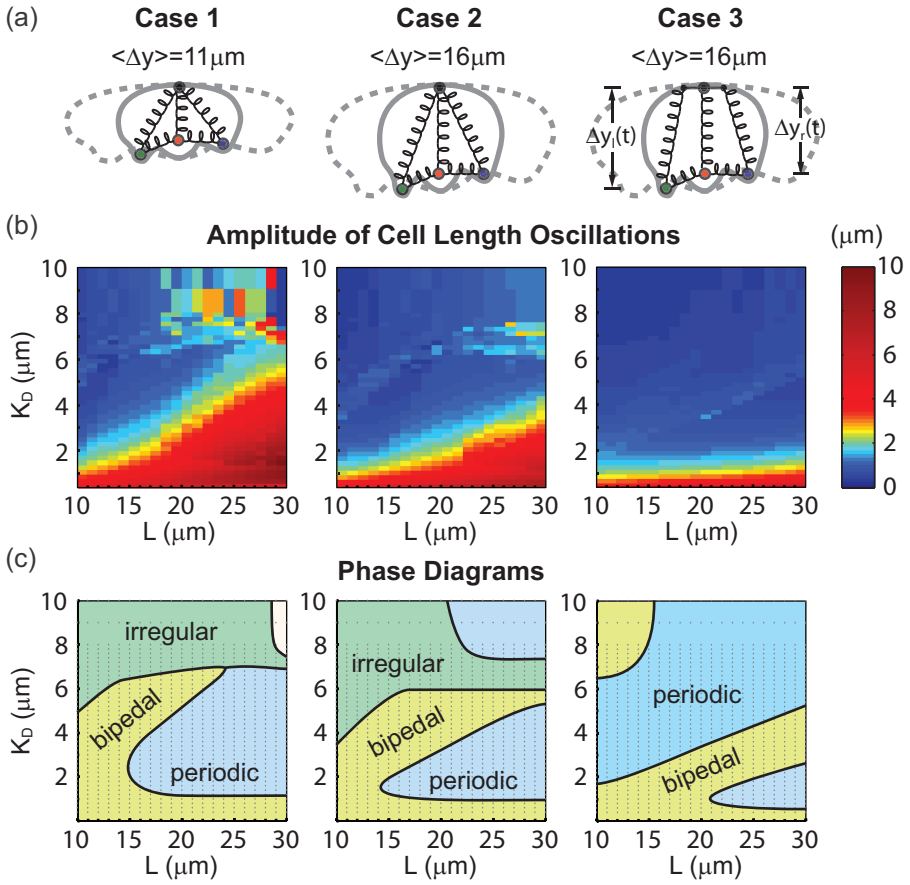

FIG. 5. (Color online) Dynamical responses of Config. 4 and the handlebar model with respect to lamellipodial elasticity, cell size, and cell aspect ratio. (a) Diagrams indicating average cell length, $\langle \Delta y \rangle$, and mechanical model: either Config. 4 (first and second columns) or the handlebar model (third column). Cell width is varied by changing spring length L. Cell length is varied by changing middle spring length, N, and then choosing lamellipodial spring length $D = D(L, K_D, N)$ such that $\langle \Delta y(t) \rangle$ remains constant. Parameter K_D sets the lamellipodial elasticity. In case 3, the length of the handle bar is set equal to L. (b) Color maps indicating the amplitude of cell length oscillations under variation of K_D and L. Saturated red (larger amplitudes occurring when K_D is relatively small) indicates amplitudes greater than those typically observed. Dark blue (smaller amplitudes occurring when K_D is relatively large) indicates amplitudes that are small and difficult to measure experimentally. Light blue and yellow (light gray shades) indicate amplitudes corresponding to realistic bipedal dynamics. Amplitude maps can be interpreted in conjunction with the corresponding phase diagrams beneath in (c). The dynamical response of the system is categorized into three behaviours: bipedal, periodic, and irregular. Bipedal regions includes both realistic and other bipedal locomotion. Both periodic and bipedal regions correspond to coherent gliding-like keratocytes, whereas irregular dynamics with anomalously large amplitudes may correspond to decoherent cells. The white region (case 1) indicates solutions where the cell fails to maintain a reasonable shape.

we find that coupling to a central element is required to generate realistic nucleus lateral displacement. This implies a mechanical landscape where the trailing edge and lamellipodium are both elastically coupled to the cell nucleus. The coupling scheme made up of all possible spring connections among the four elements (Config. 2) can generate bipedal locomotion; however, the system is not robust under parameter variation. Because this configuration is made up of more than the minimal number of springs required to maintain proper cell shape, the trailing edge elements are more sensitive to sudden motions that propagate through multiple spring pathways during stick-slip transitions. Hence, adding additional springs over-constrains the system.

Both the third and fourth configurations generate realistic bipedal dynamics including nucleus lateral displacement oscillations. In the fourth configuration, the K_D springs capture the elasticity of the lamellipodial actin cytoskeleton in the direction parallel to overall filament orientation. There is a general robustness in terms of parameter ranges over which realistic bipedal locomotion occurs, though some parameters (K_D and β) significantly modify the corresponding time-scales and amplitudes. Cell shape dynamics are highly dependent on spring constant K_D, whereas they are far less dependent on spring constant K_L. This implies that locomotion is

sensitive to elasticity of the actin cytoskeleton, but not elasticity of couplings between the trailing edge and the nucleus. Blebbistatin, a myosin II inhibitor, is known to inhibit actin network flow at the rear of keratocytes [42] but does not greatly change keratocyte stick-slip dynamics [24]. This result is consistent with our model, which predicts that cell crawling dynamics are relatively insensitive to variation of elasticity at the rear of the cell. By the same logic, the model does not contradict findings suggesting that the rear of a keratocyte is stiffer than its lamellipodium [36].

When interpreting Fig. 5, one should consider how K_D scales with cell size. Holding the elastic modulus, E, constant, one can estimate K_D as a function of cell width parameter, L, using Eq. 5. This function is obtained by solving $K_D \approx \frac{EL\Delta z_{lam}}{D(L,K_D)}$, where $D(L, K_D)$ is the spring length necessary to maintain constant cell length when L and K_D are varied. Solutions to this equation show that many limit cycles with abnormally large amplitudes in Fig. 5, cases 1 and 2, are not possible given realistic values of E and Δz_{lam}. This mechanics argument gives insight into why keratocytes are not observed with these excessively large stick-slip cycles.

In addition to recapitulating the dynamics of fast moving keratocytes, the model is also applicable to slow moving ones. The transition between slow and fast is set by parameter v_1, where in this work we have analyzed cells modelled by $v_f > v_1$. Figure S1 shows distributions representing the wide variety of cell speeds, sizes, and stick slip amplitudes recorded in fast moving keratocyte. Observed crawling dynamics can are categorized into three groups: Coherent bipedal, coherent non-bipedal, and decoherent locomotion. The model presented in this work reproduces these observations. We have shown how lamellipodial elasticity, cell size, and cell aspect ratio can determine crawling behaviour even before consideration for more complicated biological mechanisms. These findings suggest the existence of mechanically preferred cell shapes for cells that need to move quickly and efficiently. The mechanical model presented in this work should be applicable to other fan shaped cells such as gliding human fibrosarcoma cells [19] and the ameboid sperm of ascaris [51]. More complicated cell shapes and shape dynamics are possible by adding more stick-slip elements to the model. Therefore, this model may also be applicable to cells such as leukocytes and fibroblasts that undergo more complicated, highly variable, shape dynamics.

See Supplemental Material at [URL will be inserted by publisher] to find the equations of motion, experimental benchmarking, and a more detailed analysis and comparison of all four viable spring configurations. Figs. S1, S2, S3, and S4, and Movie S1 and S2 are contained in the supplemental material.

The authors thank Ms. Jingjing Wang and Mr. Angus McMullen for their critical inputs. This work was supported by NSF CMMI 0825873, and by an NSERC PGS D fellowship (AJL).

[1] E. M. Leise, Brain Res Rev **15**, 1 (1990).
[2] N. M. L. Douarin and M.-A. M. Teillet, Dev Biol **41**, 162 (1974).
[3] B. Alberts, A. Johnson, J. Lewis, M. Raff, K. Roberts, and P. Walter, "Molecular biology of the cell," (Garland Science, New York, 2002) pp. 969–982, 4th ed.
[4] C. Nathan, Nat Rev Immunol **6**, 173 (2006).
[5] V. Witko-Sarsat, P. Rieu, B. Descamps-Latscha, P. Lesavre, and L. Halbwachs-Mecarelli, Lab Invest **80**, 617 (2000).
[6] T. J. Mitchison and L. P. Cramer, Cell **84**, 371 (1996).
[7] T. D. Pollard and G. G. Borisy, Cell **112**, 453 (2003).
[8] T. Yeung, P. C. Georges, L. A. Flanagan, B. Marg, M. Ortiz, M. Funaki, N. Zahir, W. Ming, V. Weaver, and P. A. Janmey, Cell Motil Cytoskel **60**, 24 (2005).
[9] K. Keren, Z. Pincus, G. M. Allen, E. L. Barnhart, G. Marriott, A. Mogilner, and J. A. Theriot, Nature **453**, 475 (2008).
[10] C. I. Lacayo, Z. Pincus, M. M. VanDuijn, C. A. Wilson, D. A. Fletcher, F. B. Gertler, A. Mogilner, and J. A. Theriot, PLoS Biol **5**, e233 (2007).
[11] P. W. Oakes, D. C. Patel, N. A. Morin, D. P. Zitterbart, B. Fabry, J. S. Reichner, and J. X. Tang, Blood **114**, 1387 (2009).
[12] M. Herant and M. Dembo, Biophys J **98**, 1408 (2010).
[13] E. L. Barnhart, K.-C. Lee, K. Keren, A. Mogilner, and J. A. Theriot, PLoS Biol **9**, e1001059 (2011).
[14] C. A. Lemmon and L. H. Romer, Biophys J **99**, L78 (2010).
[15] A. D. Rape, W. Guo, and Y. Wang, Biomaterials **32**, 2043 (2011).
[16] A. R. Houk, A. Jilkine, C. O. Mejean, R. Boltyanskiy, E. R. Dufresne, S. B. Angenent, S. J. Altschuler, L. F. Wu, and O. D. Weiner, Cell **148**, 175 (2012).
[17] R. W. Carthew, Curr Opin Genet Dev **15**, 358 (2005).
[18] M. T. Cabeen and C. Jacobs-Wagner, Nat Rev Microbiol **3**, 601 (2005).
[19] S. Paku, J. Tovari, Z. Lorincz, F. Timar, B. Dome, L. Kopper, A. Raz, and J. Timar, Exp Cell Res **290**, 246 (2003).
[20] C. Rotsch, K. Jacobson, and M. Radmacher, P Natl Acad Sci USA **96**, 921 (1999).
[21] J. Lee, A. Ishihara, J. A. Theriot, and K. Jacobson, Nature **362**, 167 (1993).
[22] J. Lee, M. Leonard, T. Oliver, A. Ishihara, and K. Jacobson, J Cell Biol **127**, 1957 (1994).
[23] C. W. Wolgemuth, Biophys J **89**, 1643 (2005).
[24] E. L. Barnhart, G. M. Allen, F. Julicher, and J. A. Theriot, Biophys J **98**, 933 (2010).
[25] T. M. Svitkina, A. B. Verkhovsky, K. M. McQuade, and G. G. Borisy, J Cell Biol **139**, 397 (1997).
[26] M. Dembo, T. Oliver, A. Ishihara, and K. Jacobson, Biophys J **70**, 2008 (1996).
[27] M. Welch, A. Mallavarapu, J. Rosenblatt, and T. Mitchison, Curr. Opin. Cell. Bio. **9**, 54 (1997).
[28] J. A. Theriot and T. J. Mitchison, Nature **352**, 126

(1991).
[29] A. Mogilner and G. Oster, Biophys J **84**, 1591 (2003).
[30] C. Jurado, J. R. Haserick, and J. Lee, Mol Biol Cell **16**, 507 (2005).
[31] S. Deguchi, T. Ohashi, and M. Sato, J Biomech **39**, 2603 (2006).
[32] P. Marcq, N. Yoshinaga, and J. Prost, Biophys J **101**, L33 (2011).
[33] A. E. Filippov, J. Klafter, and M. Urbakh, Phys. Rev. Lett. **92**, 135503 (2004).
[34] S. Walcott and S. X. Sun, Proc Natl Acad Sci USA **107**, 7757 (2010).
[35] F. Wottawah, S. Schinkinger, B. Lincoln, R. Ananthakrishnan, M. Romeyke, J. Guck, and J. Kas, Phys Rev Lett **94**, 098103 (2005).
[36] V. M. Laurent, S. Kasas, A. Yersin, T. E. Schaffer, S. Catsicas, G. Dietler, A. B. Verkhovsky, and J.-J. Meister, Biophys J **89**, 667 (2005).
[37] F. Heinemann, H. Doschke, and M. Radmacher, Biophys J **100**, 1420 (2011).
[38] J. A. Theriot, "Theriot lab movies," `http://cmgm.stanford.edu/theriot/movies.htm` (2011).
[39] A. B. Verkhovsky, O. Y. Chaga, S. Schaub, T. M. Svitkina, J.-J. Meister, and G. G. Borisy, Mol Biol Cell **14**, 4667 (2003).
[40] T. E. Schaus, E. W. Taylor, and G. G. Borisy, Proc Natl Acad Sci USA **104**, 7086 (2007).
[41] F. Fleischer, R. Ananthakrishan, S. Eckel, H. Schmidt, J. Kas, T. M. Svitkina, V. Schmidt, and M. Beil, New J Phys **9**, 420 (2007).
[42] S. Schaub, S. Bohnet, V. M. Laurent, J.-J. Meister, and A. B. Verkhovsky, Mol Biol Cell **18**, 3723 (2007).
[43] Y. Lin, Phys Rev E **79**, 021916 (2009).
[44] K. Larripa and A. Mogilner, Physica A **372**, 113 (2006).
[45] A. Mogilner and D. W. Verzi, J Stat Phys **110**, 1169 (2003).
[46] F. Ziebert, S. Swaminathan, and I. S. Aranson, J Roy Soc Interface **(online in adv of print)**, 1 (2011).
[47] J. L. McGrath, N. J. Eungdamrong, C. I. Fisher, F. Peng, L. Mahadevan, T. J. Mitchison, and S. C. Kuo, Curr Biol **13**, 329 (2003).
[48] A. F. Straight, A. Cheung, J. Limouze, I. Chen, N. J. Westwood, J. R. Sellers, and T. J. Mitchison, Science **299**, 1743 (2003).
[49] P. T. Yam, C. A. Wilson, L. Ji, B. Hebert, E. L. Barnhart, N. A. Dye, P. W. Wiseman, G. Danuser, and J. A. Theriot, J Cell Biol **178**, 1207 (2007).
[50] M. L. Gardel, J. H. Shin, F. C. MacKintosh, L. Mahadevan, P. Matsudaira, and D. A. Weitz, Science **304**, 1301 (2004).
[51] J. E. Italiano, T. M. Roberts, M. Stewart, and C. A. Fontana, Cell **84**, 105 (1996).
[52] Z. Pincus and J. A. Theriot, J Microsc **227**, 140 (2007).
[53] P. Lenz, K. Keren, and J. A. Theriot, in *Cell Motility*, Biological and Medical Physics, Biomedical Engineering (Springer New York, 2008) pp. 31–58.

parameter	meaning	range	units	references
α	slipping drag coefficient (viscous shear)	0.15 - 0.5	$nN\,s/\mu m$	
β	sticking drag coefficient (adhesion under trailing edge)	20 - 100	$nN\,s/\mu m$	
γ	nuclear drag coefficient (adhesion under cell nucleus)	1 - 20	$nN\,s/\mu m$	
g	inertia term (sets switching time-scale between sticking and slipping)	0 - 0.8	$nNs^2/\mu m$	[24]
v_1	critical sticking velocity (upper limit of the sticking domain)	0.08	$\mu m/s$	
v_2	critical slipping velocity (lower limit of the slipping domain)	1	$\mu m/s$	
v_f	leading edge velocity ($v_f > v_1$ required for stick-slip dynamics)	0.2	$\mu m/s$	
K_N	spring constants	0 - 10	$nN/\mu m$	[24, 31, 35, 36]
K_D				
K_L				
K_W				
N	spring lengths (determines cell shape)	1 - 20	μm	
D		5 - 35		[9, 10, 24]
L		10 - 30		[52, 53]
W		18 - 60		
R	handle bar rod length	0-30	μm	

TABLE I. List of parameters used for the two dimensional model. Parameter ranges correspond to experimentally observed cell velocity, elasticity, etc. as determined by estimation or measurements reported in previous work. Each parameter range is justified by the references given here, except for rod length R, which we scale with the width of the cell's perceived leading edge. Some spring constants are not applicable depending on which configuration is used. Here, spring lengths were selected to permit proper cell shape.